Manuscript

Click here to access/download;Manuscript;manuscript_revised.pdf

Click here to view linked References

Sensitivity Analysis and Lattice Density Optimization for Sequential Inherent Strain Method used in Additive Manufacturing Process

Akihiro Takezawa[a,*], Albert To[b], Qian Chen[b], Xuan Liang[b], Florian Dugast[b], Xiaopeng Zhang[c], Mitsuru Kitamura[d]

[a] *Department of Applied Mechanics and Aerospace Engineering, School of Fundamental Science and Engineering, Waseda University, 59-311, 3-4-1 Okubo, Shinjuku-ku, Tokyo 169-8555, Japan*

[b] *Department of Mechanical Engineering and Materials Science, University of Pittsburgh, Pittsburgh, PA 15261, United States*

[c] *State Key Laboratory of Structural Analysis for Industrial Equipment, Dalian University of Technology, Dalian 116024, China*

[d] *Department of Transportation and Environmental Systems, Graduate school of Engineering, Hiroshima University, 1-4-1 Kagamiyama, Higashi-Hiroshima, Hiroshima 739-8527, Japan*

Abstract

Compensation of the thermal distortion that occurs during the fabrication process is an important issue in the field of metal additive manufacturing. Considering the problem in forming a lattice structure inside an object to reduce the thermal distortion, we developed a lattice volume fraction distribution optimization method. Assuming that the linear elastic problem is solved using the finite element method (FEM), an inherent strain method applying a layer-by-layer process utilizing the element activation during the FEM is formed as a recurrence relation, and the sensitivity of an objective function is derived based on the adjoint method. R1C1, R2C4, and R3C2: The unit

*Corresponding author. Tel: +81-3-5286-3914

Email address: atakezawa@waseda.jp (Akihiro Takezawa)

lattice shape is a simple cube with a cube or a sphere-shaped air hole, and its distribution is optimized by considering the minimum thickness of the wall surrounding it as a design variable. The effective stiffness tensor of the lattice is derived using a homogenization method. The functions of the effective properties with respect to the design variables are approximated through polynomial functions. The optimization problem is formulated as an unconstrained minimization problem. The design variables are optimized using the method of moving asymptotes. Herein, the validity of the proposed method is discussed based on quasi two-dimensional and three-dimensional numerical studies including a re-analysis through full-scale thermo-mechanical analysis.
Keywords: Additive manufacturing, Thermal distortion, Inherent strain method, Recurrence relation, Sensitivity analysis, Lattice density optimization

1. Introduction

Additive manufacturing (AM) is a novel technique realizing the fabrication of complex three-dimensional (3D) geometries through a layer-by-layer building process [1]. In particular, the development of metal AM technology has allowed the use of AM to be realized in the final industrial product beyond the prototyping of an object. Among the major approaches using metal AM, namely, powder bed fusion (PBF) and directed energy deposition (DED), metal powder is rapidly melted using a laser or electron beam and solidified layer by layer until the intended 3D shape is completed. The melting and solidification processes are similar with the welding process. Thus, as with welding, a large thermal distortion and residual stress can be an issue in metal AM [2, 3]. Techniques for the prediction and prevention of such thermal distortion are expected to be developed in the field of metal AM, particularly in the fabrication of large products.

A straightforward prediction method applied to deal with this issue is a non-linear thermo-mechanical analysis using the finite element method (FEM) when considering the temperature dependency of the physical properties and the plasticity [4, 5, 6, 7]. To simulate a stacking of the distortion, including plastic distortion, the simulation process is also divided layer by layer. The generation of a new layer is handled using the so-called element activation or element birth and death technique, which change the Young's modulus of the elements while maintaining the same state of stress as in the previous step[8, 9]. However, such a highly non-linear sequential analysis requires significant computational costs.

Although a straightforward thermo-mechanical analysis is also a major approach in a thermal distortion prediction method applied in welding[10], another low-computational cost branch, called an inherent strain method, was developed in this field. The inherent strain method was also extended to the AM simulation processes [11, 12, 13, 14, 15, 16]. In AM inherent strain methods, each layer is regarded as a basis structure generating an inherent strain. Such an inherent strain is stacked in a layer-by-layer manner using the element activation technique. The inherent strain value is calibrated by adjusting the approximated displacements and the experiment or thermo-mechanical analysis results in a simple benchmark model. The original definition of an inherent strain is the plastic strain after fabrication. However, Liang et al. [14] and Chen et al. [16] found this concept to be unsuitable for

AM and developed a modified inherent strain method including the elastic terms considering thermal relaxation and boundary effects for more accurate analysis.

On the other hand, research on topology optimization (TO) is being conducted as an effective tool generating innovative designs for AM such as strength design [17], support structure design [18, 19], fabrication cost minimization [20] and industrial applications [21, 22]. Among them, utilizing the low computational cost of the inherent strain method, when considering only the final state in the sensitivity analysis, Cheng et al. conducted a TO to prevent building failures during the final state of the AM process [19]. However, with the AM inherent strain method, the loads of the final state depend on every intermediate sequential state. Thus, this methodology is valid only in limited cases in which the thermal distortion generated by the layering process close to the final step is dominant. To optimize the thermal distortion of general problems when considering the entire layer-by-layer process, its exact formulation and sensitivity analysis are required.

As a characteristic structure of AM, the lattice structure forms regular hollow structures inside. Although the straightforward reason for using such a lattice structure is to reduce the amount of materials applied during the AM, the development of a special lattice with novel functions is an active research field in this area, such as the permeability fitting to human bones [23], the stiffness and strength [24, 25, 26, 27], the thermal conductivity [28], the negative Poisson's ratio [29, 30, 31], and a negative or extra-large thermal expansion [32, 33]. Other significant advantage is the variable lattice shape and performance like a functionally graded material [34]. Beginning with the stiffness or strength optimization [19, 35, 36, 37, 38, 39], they were extended to improvements in the anti-buckling performance [40] and vibration characteristics [41, 42], a maximization of the thermal conductivity [43, 44], and liquid cooling [45, 46]. Such an optimal functional graded lattice can reduce the thermal distortion if the stiffness is optimally distributed. Although its still limited to numerical calculation, multi-scale simultaneous optimization of lattice base shape and density distribution were also studied [47, 48].

Based on the above, we developed a lattice density distribution optimization method for suppression of the thermal distortion when assuming that the lattice structures are formed inside the target structure while maintaining the original outline using a PBF metal AM. The linear elastic problem of an inherent strain method is discretized using the FEM, and its layer-by-layer process is formed as a recurrence relation. The sensitivity of the general objective function is derived based on the adjoint method [49]. R1C1, R2C4, and R3C2: The unit lattice is assumed to be a simple cube with a cube or a sphere-shaped air hole, and its distribution is optimized by setting the minimum wall thickness as a design variable. The effective stiffness tensor of the lattice is derived using the homogenization method [50, 51]. The functions of the effective properties with respect to the design variables are approximated through polynomial functions. The optimization problem is formulated as an unconstrained minimization problem. The design variable is updated using the method of moving asymptotes (MMA) [52]. The validity of the proposed method is discussed through quasi two-dimensional (2D) and 3D numerical studies.

2. Formulation

2.1. Sequential inherent strain method for additive manufacturing

A characteristic of thermal distortion occurring during AM is warping, as shown in Fig. 1 (a), which is also observed in a usual welding process. The generation mechanism of such distortion is shown in Fig. 1 (b). The heated part during AM or welding tends to expand owing to a local high temperature. However, such an expansion is suppressed by restraining forces from the surrounding non-heated part. Because the stiffness of the melting metal is extremely low, the welded part is formed by fitting with the surrounding structure including the thermal expansion. After cooling, the welded part shrinks and tries to recover its original shape, which is smaller than that formed in a high-temperature environment. Such shrinking of the welded part is the source of the thermal distortion and residual stress. Differing from usual welding, such heating and cooling process is repeated during AM. Thus, the warping distortion can be a more serious issue in this type of manufacturing.

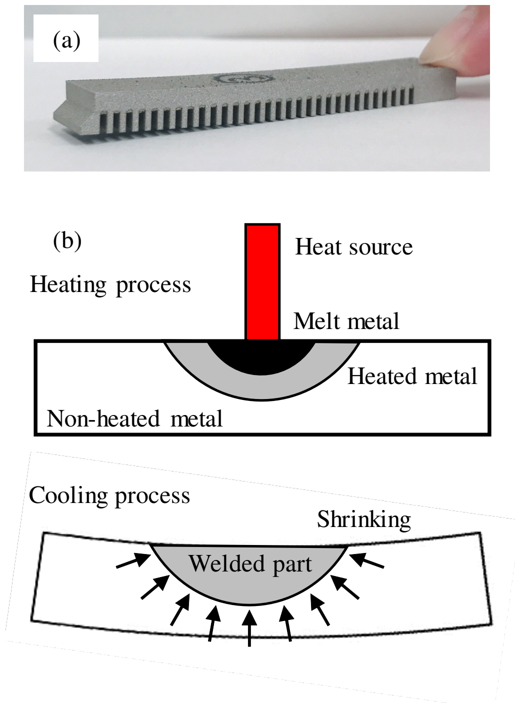

Figure 1: Warping through thermal distortion of AM part: (a) example and (b) outline of generation mechanism

As a method for predicting such thermal distortion during AM with a low computational cost, the inherent strain method has been actively studied in recent years [11, 12, 13, 14, 15, 16]. The inherent strain method was originally developed as a prediction method of the residual stress from welding [53]. The residual stress of the welding can be directly measured using an X-ray. However, because they are usually limited to the surface, irreversible cutting processes are required to capture the entire internal residual stress distribution of a thick structure. To avoid such a process, a residual stress distribution prediction method is required. The fundamental idea of the original inherent strain method used in welding is the plastic strain, which is called the inherent strain, generated through the welding process as the source of the residual stress. R2C3: This inherent strain is obtained only from the final welding state, ignoring the complicated time dependent process. i.e., the distribution of the plastic or inherent strain is assumed to depend only on the basic shape and fixed condition of the welding part. Under such an assumption, the predicted plastic strain is applied to the target structure as the initial strain in the elastic FEM. By calibrating the inherent strain value using some measurable stress, the distribution of the residual stress is numerically derived throughout the entire structure. Another aspect of the inherent strain method is a low-cost computational method predicting the thermal deformation of the welded structure. Under the assumption that the inherent strain only depends on the basic shape of the welding parts, by referring to the database of the inherent strain corresponding to the basic welding patterns, the thermal distortion of a body composed of several welding parts can be predicted [54, 55]. Such a low computational cost can also be utilized in studies on the manufacturing sequence [56].

R2C3: Such application of the inherent strain method to the manufacturing sequence led to the AM inherent strain method. In the simplest AM inherent strain method, each layer is regarded as a basis unit generating an inherent strain [11, 12, 13, 15]. That is, each layer has a uniform inherent strain toward the shrinking direction ignoring time-transient process of its fabrication. A warping deformation can be represented by a combination of the inherent strain and element activation technique [8, 9] applied through the FEM. In a welding analysis utilizing an element activation, the entire FEM model is constructed and represents the generation of the structure by changing the Young's modulus. That is, the Young's modulus of the activating elements is increased from a small value with zero stress. An extremely small Young's modulus is set to the deactivated layer elements to avoid a singularity. The outline of the process is shown in Fig. 2. To explain this process, two simplified layers are formed on the base plate. During the initial step, only the first layer is formed and the second layer is deactivated. During the second step, the inherent strain is applied to the first layer. During the third step, the second layer is activated. Through this step, if only the Young's modulus is changed, the equilibrium equation is calculated using the new increased Young's modulus and the deformation of the first layer is reduced because the total stiffness of the structure is simply increased over the given load. Such phenomena never occur during an actual process. To form a new layer on the deformed layer while keeping the same deformation, the Young's modulus of the new layer must be increased with zero stress. That is, the expected stress is canceled by adding strain of the current layer generated in a deactivating state as an initial strain. During the fourth step, the inherent strain is applied to the second layer. Finally, the second layer suffers from shrinking forces through activation and the inherent strain. After cutting from the base plate, this two-layer structure bends toward an imbalance of the internal force. To use such a process for the prediction of the thermal distortion in the AM, the inherent strain value must be calibrated based on the experiment results or the detailed thermo-mechanical FEM results.

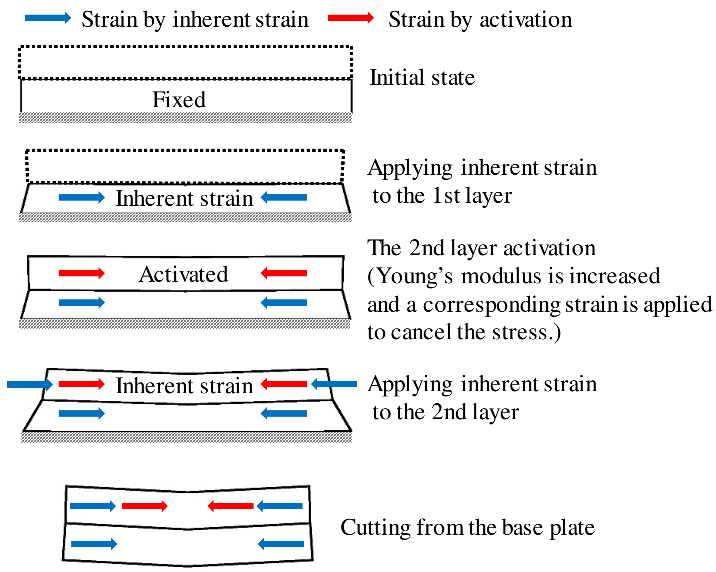

Figure 2: Outline of the sequential layer-by-layer process of the AM inherent strain method representing a warping deformation.

In one of the latest AM inherent strain methods, Liang et al. [14] and Chen et al. [16] developed a more accurate way to extract the inherent strains from detailed process simulation by considering elastic contribution. R2C2: Moreover, varying lattice density can affect the inherent strain value because the laser pass can change according to the lattice geometry change. However, in this study, for simplicity, we use a conventional AM inherent strain method, assuming that the inherent strain value is identical throughout the entire structure, independent of the lattice density distribution.

2.2. Recurrence relation representation of layer-by-layer process

R2C3: In the AM inherent strain method, a stack of inherent strains and activation forces is usually handled using time transient FEM solvers. However, the AM inherent strain method is actually an approximated physical problem and is not affected by the time scale. In other words, it is enough to repeat the static analysis considering the mutual effect without the time transient effect. We regard a recurrent formula as appropriate for representing the current state depending on the previous state during the repeated process without the actual time scale. Thus, in this study, the exact formulation of the AM inherent strain method is derived as a recurrent formula as follows.

First, a recurrent formula representing the change in displacement of an elastic body with a varying stiffness through the generation of a new layer, as well as the cutting from the plate and a varying force occurring through the inherent strain and layer activation, is derived. Considering the linear elastic problem discretized using the FEM, the equilibrium equation at the n-th step is as follows:

$$\mathbf{K}_n\mathbf{u}_n = \mathbf{f}_n, \tag{1}$$

where $\mathbf{K}$, $\mathbf{u}$, and $\mathbf{f}$ are the stiffness matrix, the displacement vector, and the force vector. The increment on both sides is represented as follows:

$$\begin{aligned} &\Delta(\mathbf{K}_n\mathbf{u}_n) - \Delta\mathbf{f}_n \\ =&\Delta\mathbf{K}_n\mathbf{u}_{n+1} + \mathbf{K}_n\Delta\mathbf{u}_n - \Delta\mathbf{f}_n \\ =&\Delta\mathbf{K}_n\mathbf{u}_{n+1} + \mathbf{K}_n(\mathbf{u}_{n+1} - \mathbf{u}_n) - \Delta\mathbf{f}_n \\ =&(\mathbf{K}_n + \Delta\mathbf{K}_n)\mathbf{u}_{n+1} - \mathbf{K}_n\mathbf{u}_n - \Delta\mathbf{f}_n \\ =&\mathbf{0} \end{aligned} \tag{2}$$

where $\Delta(\mathbf{K}_n\mathbf{u}_n) = \Delta\mathbf{K}_n\mathbf{u}_{n+1} + \mathbf{K}_n\Delta\mathbf{u}_n$ and $\Delta\mathbf{u}_n = \mathbf{u}_{n+1} - \mathbf{u}_n$. Here, the n-th load increment $\Delta\mathbf{f}_n$ can be divided as $\Delta\mathbf{f}_n = \Delta\mathbf{f}_n^{\text{act}} + \Delta\mathbf{f}_n^{\text{ihs}}$, where $\Delta\mathbf{f}_n^{\text{act}}$

is the load increment through the activation, and $\mathbf{f}_n^{\mathrm{ihs}}$ is that of the inherent strain. In addition, $\Delta\mathbf{f}_n^{\mathrm{ihs}}$ is defined as follows:

$$\Delta\mathbf{f}_n^{\mathrm{ihs}} = \mathbf{H}_{n+1}^{\mathrm{ihs}}\mathbf{K}_{n+1}\mathbf{u}_n^{\mathrm{ihs}} \tag{3}$$

where $\mathbf{H}^{\mathrm{ihs}}$ and $\mathbf{u}^{\mathrm{ihs}}$ are the 0-1 matrix specifying nodes in which the loads corresponding to inherent strains is applied and the fixed displacement vector corresponding to the inherent strain at the specified step, respectively. However, $\Delta\mathbf{f}_n^{\mathrm{ihs}}$ does not depend on the state variable displacement, whereas $\Delta\mathbf{f}_n^{\mathrm{act}}$ does depend on the displacements of the previous step.

An element activation is a key technique of the AM-inherent strain method, as shown in Fig. 2. With this method, the generation of the structure is represented by changing the Young's modulus with a zero-stress state. The zero-stress state of the activated elements is realized by adding the initial strain to these elements corresponding to the former state displacement, thereby canceling the stress generated by the change in the Young's modulus. In Eq. (2), the load increment through activation at the $n+1$-th step is formulated as follows:

$$\Delta\mathbf{f}_n^{\mathrm{act}} = \mathbf{H}_{n+1}^{\mathrm{act}}\Delta\mathbf{K}_n\mathbf{u}_n \tag{4}$$

where $\mathbf{H}^{\mathrm{act}}$ is the 0-1 matrix specifying the nodes corresponding to activated elements at the specified step. Substituting Eqs. (3) and (4) into Eq. (2),

$$
\begin{aligned}
&(\mathbf{K}_n + \Delta\mathbf{K}_n)\mathbf{u}_{n+1} - \mathbf{K}_n\mathbf{u}_n - \mathbf{H}^{\mathrm{act}}_{n+1}\Delta\mathbf{K}_n\mathbf{u}_n - \mathbf{H}^{\mathrm{ihs}}_{n+1}\mathbf{K}_{n+1}\mathbf{u}^{\mathrm{ihs}}_{n+1} \\
=&\{\mathbf{K}_n + (\mathbf{I} - \mathbf{H}^{\mathrm{act}}_{n+1})\Delta\mathbf{K}_n + \mathbf{H}^{\mathrm{act}}_{n+1}\Delta\mathbf{K}_n\}\mathbf{u}_{n+1} - \mathbf{K}_n\mathbf{u}_n - \mathbf{H}^{\mathrm{act}}_{n+1}\Delta\mathbf{K}_n\mathbf{u}_n - \mathbf{H}^{\mathrm{ihs}}_{n+1}\mathbf{K}_{n+1}\mathbf{u}^{\mathrm{ihs}}_{n+1} \\
=&(\mathbf{I} - \mathbf{H}^{\mathrm{act}}_{n+1})\Delta\mathbf{K}_n\mathbf{u}_{n+1} + (\mathbf{K}_n + \mathbf{H}^{\mathrm{act}}_{n+1}\Delta\mathbf{K}_n)(\mathbf{u}_{n+1} - \mathbf{u}_n) - \mathbf{H}^{\mathrm{ihs}}_{n+1}\mathbf{K}_{n+1}\mathbf{u}^{\mathrm{ihs}}_{n+1} \\
=&(\mathbf{I} - \mathbf{H}^{\mathrm{act}}_{n+1})\Delta\mathbf{K}_n\mathbf{u}_{n+1} + (\mathbf{K}_n + \mathbf{H}^{\mathrm{act}}_{n+1}\Delta\mathbf{K}_n)\Delta\mathbf{u}_n - \mathbf{H}^{\mathrm{ihs}}_{n+1}\mathbf{K}_{n+1}\mathbf{u}^{\mathrm{ihs}}_{n+1} \\
=&\mathbf{0}
\end{aligned}
\tag{5}
$$

That is, the recurrent formula representing the displacement at the n-th step is obtained as follows:

$$\mathbf{A}_n\mathbf{u}_n + \mathbf{B}_n\Delta\mathbf{u}_{n-1} - \mathbf{H}^{\mathrm{ihs}}_n\mathbf{K}_n\mathbf{u}^{\mathrm{ihs}}_n = \mathbf{0} \tag{6}$$

$$\mathbf{u}_0 = \mathbf{0} \tag{7}$$

where $\mathbf{A}_n = (\mathbf{I} - \mathbf{H}^{\mathrm{act}}_n)\Delta\mathbf{K}_{n-1}$ and $\mathbf{B}_n = \mathbf{K}_{n-1} + \mathbf{H}^{\mathrm{act}}_n\Delta\mathbf{K}_{n-1}$. The reason the increment $\Delta\mathbf{u}_{n-1}$ is introduced instead of $\mathbf{u}_{n-1}$ is this is suitable in the following sensitivity analysis.

2.3. Sensitivity analysis

The sensitivity of the following general objective function is represented as a fixed sum of a function with respect to the displacement vector $\mathbf{u}$ based on the adjoint method [49].

$$g = \sum_{i=1}^{N} h_i(\mathbf{u}_i) \tag{8}$$

The Lagrangian is obtained from Eqs. (6) and (8) as follows:

$$L = \sum_{i=1}^{N} h_i(\mathbf{u}_i) + \sum_{i=1}^{N} \boldsymbol{\lambda}_i^T \left(\mathbf{A}_i\mathbf{u}_i + \mathbf{B}_i\Delta\mathbf{u}_{i-1} - \mathbf{H}^{\mathrm{ihs}}_i\mathbf{K}_i\mathbf{u}^{\mathrm{ihs}}_i\right), \tag{9}$$

where $\boldsymbol{\lambda}$ is the adjoint variable vector.

Based on the chain rule, the derivative of L with respect to the design variable x is obtained as follows:

$$\frac{\mathrm{d}L}{\mathrm{d}x} = \frac{\partial L}{\partial x} + \sum_{i=1}^{N} \left(\frac{\partial L}{\partial \mathbf{u}_i} \frac{\mathrm{d}\mathbf{u}_i}{\mathrm{d}x} + \frac{\partial L}{\partial \Delta \mathbf{u}_{i-1}} \frac{\mathrm{d}\Delta \mathbf{u}_{i-1}}{\mathrm{d}x} \right) \tag{10}$$

Calculating each term,

$$\frac{\partial L}{\partial x} = \sum_{i=1}^{N} \frac{\partial h_i}{\partial x} + \sum_{i=1}^{N} \boldsymbol{\lambda}_i^T \left(\frac{\partial \mathbf{A}_i}{\partial x} \mathbf{u}_i + \frac{\partial \mathbf{B}_i}{\partial x} \Delta \mathbf{u}_{i-1} - \mathbf{H}_i^{\text{ihs}} \frac{\partial \mathbf{K}_i}{\partial x} \mathbf{u}_i^{\text{ihs}} \right) \tag{11}$$

$$\sum_{i=1}^{N} \frac{\partial L}{\partial \mathbf{u}_i} \frac{\mathrm{d}\mathbf{u}_i}{\mathrm{d}x} = \sum_{i=1}^{N} \frac{\partial h_i}{\partial \mathbf{u}_i} \frac{\mathrm{d}\mathbf{u}_i}{\mathrm{d}x} + \sum_{i=1}^{N} \boldsymbol{\lambda}_i^T \mathbf{A}_i \frac{\mathrm{d}\mathbf{u}_i}{\mathrm{d}x} \tag{12}$$

$$\sum_{i=1}^{N} \frac{\partial L}{\partial \Delta \mathbf{u}_{i-1}} \frac{\mathrm{d}\Delta \mathbf{u}_{i-1}}{\mathrm{d}x} = \sum_{i=1}^{N} \boldsymbol{\lambda}_i^T \mathbf{B}_i \frac{\mathrm{d}\Delta \mathbf{u}_{i-1}}{\mathrm{d}x} \tag{13}$$

Substituting Eqs. (11)-(13) into Eq. (10),

$$\begin{aligned} \frac{\mathrm{d}L}{\mathrm{d}x} &= \sum_{i=1}^{N} \frac{\partial h_i}{\partial x} + \sum_{i=1}^{N} \boldsymbol{\lambda}_i^T \left(\frac{\partial \mathbf{A}_i}{\partial x} \mathbf{u}_i + \frac{\partial \mathbf{B}_i}{\partial x} \Delta \mathbf{u}_{i-1} - \mathbf{H}_i^{\text{ihs}} \frac{\partial \mathbf{K}_i}{\partial x} \mathbf{u}_i^{\text{ihs}} \right) \\ &\quad + \sum_{i=1}^{N} \frac{\partial h_i}{\partial \mathbf{u}_i} \frac{\mathrm{d}\mathbf{u}_i}{\mathrm{d}x} + \sum_{i=1}^{N} \boldsymbol{\lambda}_i^T \mathbf{A}_i \frac{\mathrm{d}\mathbf{u}_i}{\mathrm{d}x} + \sum_{i=1}^{N} \boldsymbol{\lambda}_i^T \mathbf{B}_i \frac{\mathrm{d}\Delta \mathbf{u}_{i-1}}{\mathrm{d}x} \\ &= \sum_{i=1}^{N} \frac{\partial h_i}{\partial x} + \sum_{i=1}^{N} \boldsymbol{\lambda}_i^T \left(\frac{\partial \mathbf{A}_i}{\partial x} \mathbf{u}_i + \frac{\partial \mathbf{B}_i}{\partial x} \Delta \mathbf{u}_{i-1} - \mathbf{H}_i^{\text{ihs}} \frac{\partial \mathbf{K}_i}{\partial x} \mathbf{u}_i^{\text{ihs}} \right) \\ &\quad + \sum_{i=1}^{N} \left(\frac{\partial h_i}{\partial \mathbf{u}_i} + \boldsymbol{\lambda}_i^T \mathbf{A}_i \right) \frac{\mathrm{d}\mathbf{u}_i}{\mathrm{d}x} + \sum_{i=1}^{N} \boldsymbol{\lambda}_i^T \mathbf{B}_i \frac{\mathrm{d}\Delta \mathbf{u}_{i-1}}{\mathrm{d}x} \end{aligned} \tag{14}$$

The sum of the third and fourth terms of Eq. (14) will be equal to zero by an appropriate determination of the adjoint variable. Here, a rule of product differentiation, $\Delta(u_n v_n) = \Delta u_n v_{n+1} + u_n \Delta v_n$, is considered, where u and v are arbitrary functions. Thus, a formula for a fixed summation by parts is obtained as $\sum_{i=1}^{N} \Delta u_i v_i = u_{N+1} v_{N+1} - u_1 v_1 - \sum_{i=1}^{N} u_{i+1} \Delta v_i$. Thus, the fourth term of Eq. (14) is expanded as follows:

$$\begin{aligned}\sum_{i=1}^{N} \boldsymbol{\lambda}_i^T \mathbf{B}_i \frac{\mathrm{d}\Delta \mathbf{u}_{i-1}}{\mathrm{d}x} &= \boldsymbol{\lambda}_{N+1}^T \mathbf{B}_{N+1} \frac{\mathrm{d}\mathbf{u}_N}{\mathrm{d}x} - \boldsymbol{\lambda}_1^T \mathbf{B}_1 \frac{\mathrm{d}\mathbf{u}_0}{\mathrm{d}x} - \sum_{i=1}^{N} \Delta(\boldsymbol{\lambda}_i^T \mathbf{B}_i) \frac{\mathrm{d}\mathbf{u}_i}{\mathrm{d}x} \\ &= \boldsymbol{\lambda}_{N+1}^T \mathbf{B}_{N+1} \frac{\mathrm{d}\mathbf{u}_N}{\mathrm{d}x} - \boldsymbol{\lambda}_1^T \mathbf{B}_1 \frac{\mathrm{d}\mathbf{u}_0}{\mathrm{d}x} - \sum_{i=1}^{N} (\Delta \boldsymbol{\lambda}_i^T \mathbf{B}_{i+1} + \boldsymbol{\lambda}_i^T \Delta \mathbf{B}_i) \frac{\mathrm{d}\mathbf{u}_i}{\mathrm{d}x}\end{aligned} \tag{15}$$

The sum of the third and fourth terms of Eq. (14) is as follows:

$$\begin{aligned}&\sum_{i=1}^{N} \left(\frac{\partial h_i}{\partial \mathbf{u}_i} + \boldsymbol{\lambda}_i^T \mathbf{A}_i \right) \frac{\mathrm{d}\mathbf{u}_i}{\mathrm{d}x} + \sum_{i=1}^{N} \boldsymbol{\lambda}_i^T \mathbf{B}_i \frac{\mathrm{d}\Delta \mathbf{u}_{i-1}}{\mathrm{d}x} \\ =&\sum_{i=1}^{N} \left(\frac{\partial h_i}{\partial \mathbf{u}_i} + \boldsymbol{\lambda}_i^T \mathbf{A}_i \right) \frac{\mathrm{d}\mathbf{u}_i}{\mathrm{d}x} + \boldsymbol{\lambda}_{N+1}^T \mathbf{B}_{N+1} \frac{\mathrm{d}\mathbf{u}_N}{\mathrm{d}x} - \boldsymbol{\lambda}_1^T \mathbf{B}_1 \frac{\mathrm{d}\mathbf{u}_0}{\mathrm{d}x} - \sum_{i=1}^{N} (\Delta \boldsymbol{\lambda}_i^T \mathbf{B}_{i+1} + \boldsymbol{\lambda}_i^T \Delta \mathbf{B}_i) \frac{\mathrm{d}\mathbf{u}_i}{\mathrm{d}x} \\ =&\sum_{i=1}^{N} \left(\frac{\partial h_i}{\partial \mathbf{u}_i} + \boldsymbol{\lambda}_i^T \mathbf{A}_i - \Delta \boldsymbol{\lambda}_i^T \mathbf{B}_{i+1} - \boldsymbol{\lambda}_i^T \Delta \mathbf{B}_i \right) \frac{\mathrm{d}\mathbf{u}_i}{\mathrm{d}x} + \boldsymbol{\lambda}_{N+1}^T \mathbf{B}_{N+1} \frac{\mathrm{d}\mathbf{u}_N}{\mathrm{d}x} - \boldsymbol{\lambda}_1^T \mathbf{B}_1 \frac{\mathrm{d}\mathbf{u}_0}{\mathrm{d}x} \\ =&\sum_{i=1}^{N} \left\{ \frac{\partial h_i}{\partial \mathbf{u}_i} + \boldsymbol{\lambda}_i^T (\mathbf{I} - \mathbf{H}_i^{\mathrm{act}}) \Delta \mathbf{K}_{n-1} - \Delta \boldsymbol{\lambda}_i^T (\mathbf{K}_i + \mathbf{H}_{i+1}^{\mathrm{act}} \Delta \mathbf{K}_i) - \boldsymbol{\lambda}_i^T \Delta (\mathbf{K}_{i-1} + \mathbf{H}_i^{\mathrm{act}} \Delta \mathbf{K}_{i-1}) \right\} \frac{\mathrm{d}\mathbf{u}_i}{\mathrm{d}x} \\ &+ \boldsymbol{\lambda}_{N+1}^T \mathbf{B}_{N+1} \frac{\mathrm{d}\mathbf{u}_N}{\mathrm{d}x} - \boldsymbol{\lambda}_1^T \mathbf{B}_1 \frac{\mathrm{d}\mathbf{u}_0}{\mathrm{d}x} \\ =&\sum_{i=1}^{N} \left\{ \frac{\partial h_i}{\partial \mathbf{u}_i} + \boldsymbol{\lambda}_i^T \mathbf{K}_i - \boldsymbol{\lambda}_{i+1}^T (\mathbf{K}_i + \mathbf{H}_{i+1}^{\mathrm{act}} \Delta \mathbf{K}_i) \right\} \frac{\mathrm{d}\mathbf{u}_i}{\mathrm{d}x} + \boldsymbol{\lambda}_{N+1}^T \mathbf{B}_{N+1} \frac{\mathrm{d}\mathbf{u}_N}{\mathrm{d}x} - \boldsymbol{\lambda}_1^T \mathbf{B}_1 \frac{\mathrm{d}\mathbf{u}_0}{\mathrm{d}x}\end{aligned} \tag{16}$$

Because $\dfrac{\mathrm{d}\mathbf{u}_0}{\mathrm{d}x}$ is zero from the initial condition in Eq. (7), when the above equation is continuously zero, the following adjoint equation must be satisfied.

$$\frac{\partial h_n}{\partial \mathbf{u}_n} + \boldsymbol{\lambda}_n^T \mathbf{K}_n - \boldsymbol{\lambda}_{n+1}^T (\mathbf{K}_n + \mathbf{H}_{n+1}^{\mathrm{act}} \Delta \mathbf{K}_n) = 0 \tag{17}$$

$$\boldsymbol{\lambda}_{N+1}^T = 0 \tag{18}$$

Finally, the sensitivity is obtained as follows by simplifying Eq. (14):

$$\begin{aligned}\frac{dL}{dx} &= \sum_{i=1}^{N}\left[\frac{\partial h_i}{\partial x} + \boldsymbol{\lambda}_i^T\left\{(\mathbf{I}-\mathbf{H}_i^{\mathrm{act}})\frac{\partial \Delta\mathbf{K}_{i-1}}{\partial x}\mathbf{u}_i + \left(\frac{\partial \mathbf{K}_{i-1}}{\partial x} + \mathbf{H}_i^{\mathrm{act}}\frac{\partial \Delta\mathbf{K}_{i-1}}{\partial x}\right)(\mathbf{u}_i - \mathbf{u}_{i-1})\right.\right.\\ &\qquad \left.\left. - \mathbf{H}_i^{\mathrm{ihs}}\frac{\partial \mathbf{K}_i}{\partial x}\mathbf{u}_i^{\mathrm{ihs}}\right\}\right]\\ &= \sum_{i=1}^{N}\left[\frac{\partial h_i}{\partial x} + \boldsymbol{\lambda}_i^T\left\{\frac{\partial \mathbf{K}_i}{\partial x}\mathbf{u}_i - \left(\frac{\partial \mathbf{K}_{i-1}}{\partial x} + \mathbf{H}_i^{\mathrm{act}}\frac{\partial \Delta\mathbf{K}_{i-1}}{\partial x}\right)\mathbf{u}_{i-1} - \mathbf{H}_i^{\mathrm{ihs}}\frac{\partial \mathbf{K}_i}{\partial x}\mathbf{u}_i^{\mathrm{ihs}}\right\}\right]\end{aligned} \tag{19}$$

2.4. Lattice optimization problem

Figure 3 shows the outline of the design target. We assume that a structure filled with lattices is built using an AM in a layer-by-layer process. The density distribution of the lattices is optimized. The optimization process of the lattice density can use similar algorithm as that applied using TO [57, 58]. In TO, a intermediate density between zero and 1 is unfavored because the density distribution is originally the 0-1 discrete function. The solid isotropic material with penalization (SIMP) is usually used to penalize the intermediate density. However, an intermediate value of the density function is considered as the effective density of a lattice with a corresponding geometry in lattice optimization. The effective properties corresponding to representative densities are calculated and then interpolated using polynomial functions before optimization. This is a common way in deriving the function of the effective properties of a lattice with respect to the lattice density [36, 41, 43]. The representative size of a lattice is mapped into the interval $[0, 1]$ as a function of a formulated as a function of the design variable d.

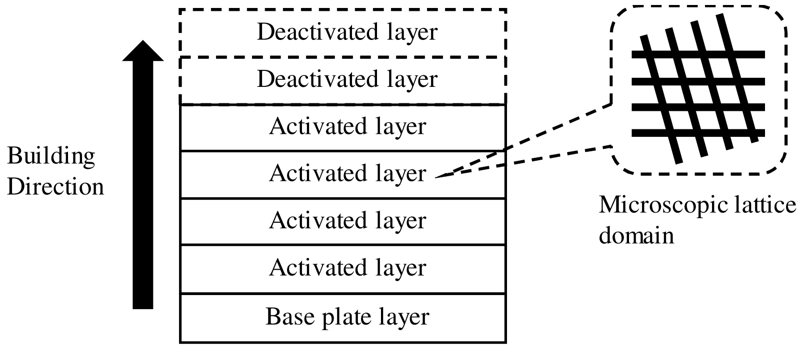

Figure 3: Outline of the design target domain.

The advantage of the proposed method is being able to consider the optimization problem of the thermal distortion in an arbitrary step of the inherent strain layer-by-layer process. Thus, as a general objective function, the sum of the square norm of the specified displacements of each step is applied. The objective function is derived from the recurrence relation in Eqs. (6) and (7). The stiffness matrix $\mathbf{K}$ is considered as a function of the design variable vector $\mathbf{d}$ ($\mathbf{0} \leq \mathbf{d} \leq \mathbf{1}$) whose dimension is equal to the number of lattices. The optimization problem is then defined as follows:

$$\text{minimize} \ \sum_{i=1}^{N} |\mathbf{H}_i^{\mathrm{obj}} \mathbf{u}_i|^2, \tag{20}$$

subject to

$$\begin{gathered} \text{Eqs. (6) and (7)}, \\ \mathbf{0} \leq \mathbf{d} \leq \mathbf{1}, \end{gathered} \tag{21}$$

where N is the number of steps and $\mathbf{H}_i^{\mathrm{obj}}$ is a 0-1 matrix specifying the displacements considered in the objective function at the i-th step.

3. Numerical implementation

3.1. Lattice base shape and effective properties

R1C1, R2C4, and R3C2: Simple shapes shown in Fig. 4 are introduced as a basic unit lattice geometry in this study. A cube (Case A) or a sphere (Case B) void is introduced into a cube unit cell, and the minimum thickness is varied during the optimization process. Six 1 mm diameter holes are introduced to remove the remaining powder from the PBF process. The unit cell length is set to be 5 mm. The Case A lattice is suitable for voxel mesh discretization used in the full scale thermo-mechanical analysis, while Case B is suitable for actual fabrication because it has fewer horizontal overhangs.

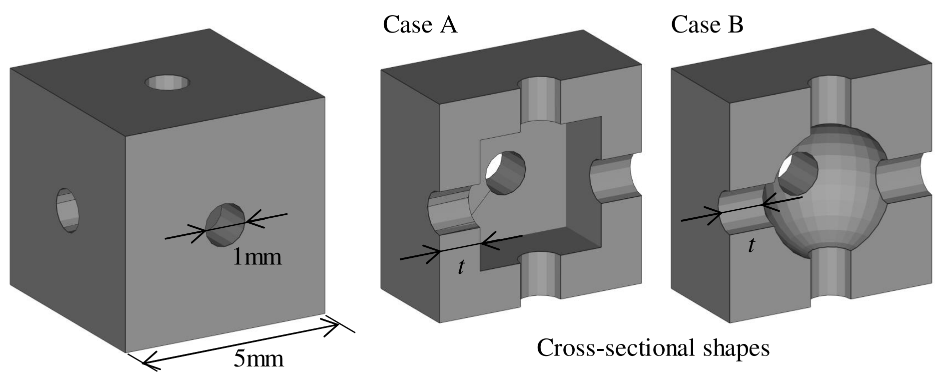

Figure 4: R1C1, R2C4 and R3C2: Basis shapes of the unit lattices.

The effective properties of the lattice are derived by using numerical homogenization [50, 51] based on the FEM. R2C1: The developed lattice is assumed to be laid out periodically. The design target is the geometry of the lattice base cell. The static–elastic deformation of a metal with isotropic stiffness is considered first to calculate the effective lattice stiffness. The microscale linear elastic deformation of the lattice structure is assumed to follow Hooke's law:

$$\sigma_{ij} = C_{ijkl}\epsilon_{kl} = C_{ijkl}\frac{\partial u_k}{\partial x_l}, \tag{22}$$

where $\boldsymbol{\sigma}$, $\mathbf{C}$, $\boldsymbol{\epsilon}$, and $\mathbf{u}$ are, respectively, the stress tensor, elastic tensor, strain tensor, and displacement vector. i, j, k, and l are the indices of the tensors. By solving this equation numerically using FEM with Dirichlet boundary conditions ($\mathbf{u} = \mathbf{0}$), the distribution of displacements $\mathbf{u}$ in the internal structure is obtained.

The effective elastic tensor $\mathbf{C}^H$ of the periodic structure that is composed of a unit cell Y is,

$$C^H_{ijkl} = \frac{1}{|Y|}\int_Y \left(C_{ijkl} - C_{ijpq}\frac{\partial \chi_p^{kl}}{\partial y_q} \right) \mathrm{d}Y, \tag{23}$$

where $\boldsymbol{\chi}$ is the displacement obtained by solving the problem of Y periodic cells, and p and q are the dummy indices,

$$\int_Y C_{ijpq}\left(\delta_{pk}\delta_{ql} - \frac{\partial \chi_p^{kl}}{\partial y_q} \right) \frac{\partial v_i}{\partial y_j}\mathrm{d}Y = 0. \tag{24}$$

Here, $\mathbf{v}$ is an arbitrary test function, and δ is the Kronecker delta.

Representative values are calculated using a wall thickness with $t = 0.25$ to 2 mm at 0.5 mm intervals. The thickness t ($0.5 \leq t \leq 2$) is mapped into the design variable d ($0 \leq d \leq 1$) by $t = 0.5 + 1.5d$ for the ease of optimization. These representative values are interpolated using the polynomial function with respect to the design variable d. Inconel 718 with a Young's modulus of $E = 208$GPa and a Poisson's ratio of 0.3 is the assumed material. The interpolation functions of the effective elastic tensor and volume fraction are summarized in Fig. 5. Because the miller symmetry of the cell is guaranteed, the three components of the effective elastic tensor are independent.

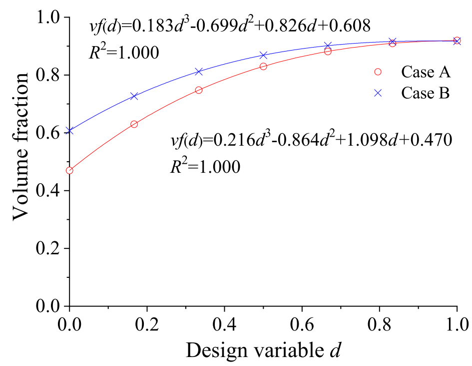

(a)

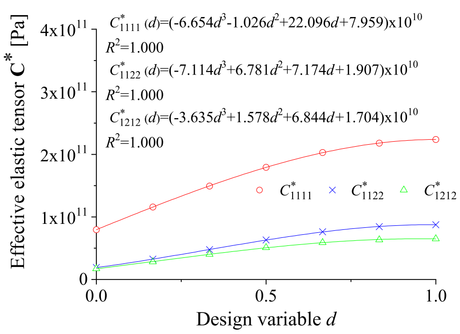

(b)

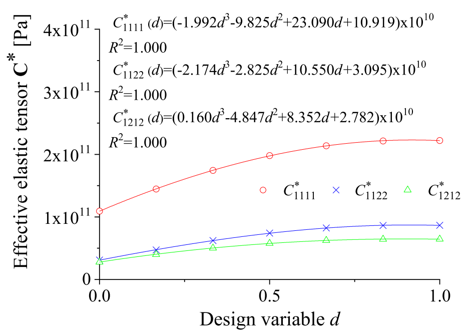

(c)

Figure 5: R1C1, R2C4, and R3C2: Interpolation functions of (a) volume fraction and effective elastic tensor of (b) Case A lattice and (c) Case B lattice with respect to the design variable. R^2 is the coefficient of determination.

3.2. Optimization procedure

The design variable d is updated using the MMA, a gradient-based algorithm [52]. Figure 6 shows a flowchart. R2C1: Before optimization, the approximation functions between the effective stiffness and the design variable d shown in Fig. 5 is built using the homogenization method and initial values of d are set. During optimization, the effective stiffness of the lattices are first calculated using the approximation in Fig. 5. The recurrence relation of the inherent strain method in Eq. (6) is calculated using the FEM. The objective function and constraint are then calculated. Subsequently, the adjoint variable is derived by solving the recurrence relation in Eq. (17) and (18). The sensitivities of the objective function are then calculated through Eq. (19). The design variables are finally updated using the MMA [52]. These procedures are repeated until a specified convergence criteria is satisfied.

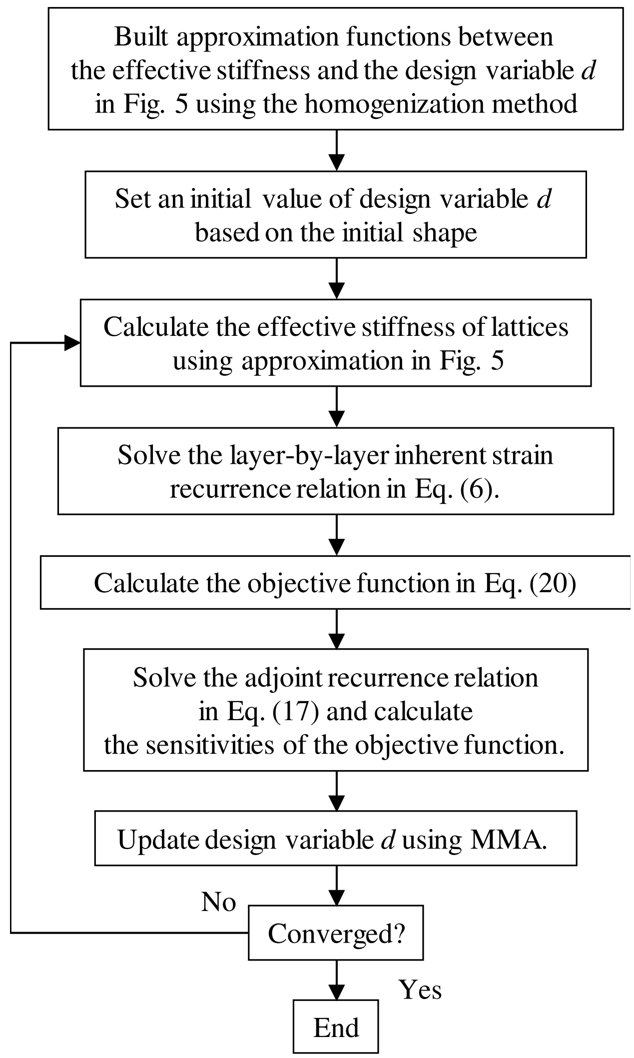

Figure 6: R2C1: Flowchart of optimization procedure.

4. Numerical example

Quasi-2D and 3D examples are studied to validate the proposed method. FEM calculations for solving the recurrent formula were conducted using COMSOL Multiphysics software. Finite-element formulations are linear Lagrange elements. The design target structures are assumed to be formed by a PBF metal AM. The material is assumed to be the same Inconel 718 with a Young's modulus of $E = 208$ GPa and a Poisson's ratio of 0.3 with the one used in the derivation of the interpolation functions. The coefficient of the Young's modulus of the deactivated material is set to 10^{-5}.

4.1. Quasi 2D example

A rectangular plate, shown in Fig. 7, is used as the first basic example. We imagine the fabrication of a 50 mm $\times$ 200 mm plate part with a 5 mm thickness composed of ten inherent strain layers. The bottom 5 mm layer is assumed to be a base plate with a fully dense material. Considering the post-processing cutting of the bottom of the part after fabrication, excluding the left bottom part, we evaluate the sum of the square of the vertical displacements of the top and bottom planes. The analysis domain is one-half when considering the symmetry. The domain is discretized by a 5 mm lattice, as shown in Fig. 4. That is, the part domain is composed of 10 $\times$ 20 lattices. The analysis domain is also discretized by a 5 mm cube voxel mesh. In the part layers, one lattice corresponds with one finite element. The design variables are set to each lattice.

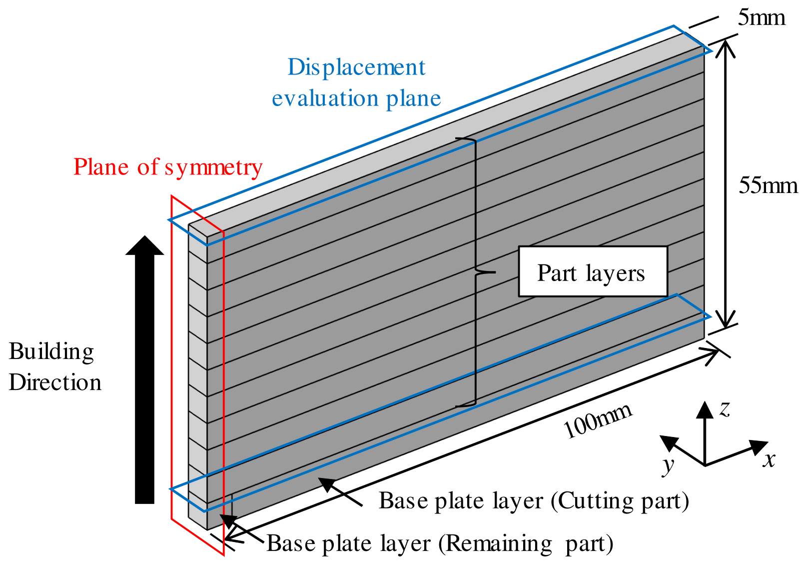

Figure 7: The outline of the design target of the quasi 2D example.

With the inherent strain method, the inherent strain is applied to the one-level down layer of the activated layer [12]. Figure 8 shows the extracted inherent strain processes from the initial to the final steps. At the final step, cutting is represented by deactivating the base plate layer except for the left corner. A warping deformation was clearly observed.

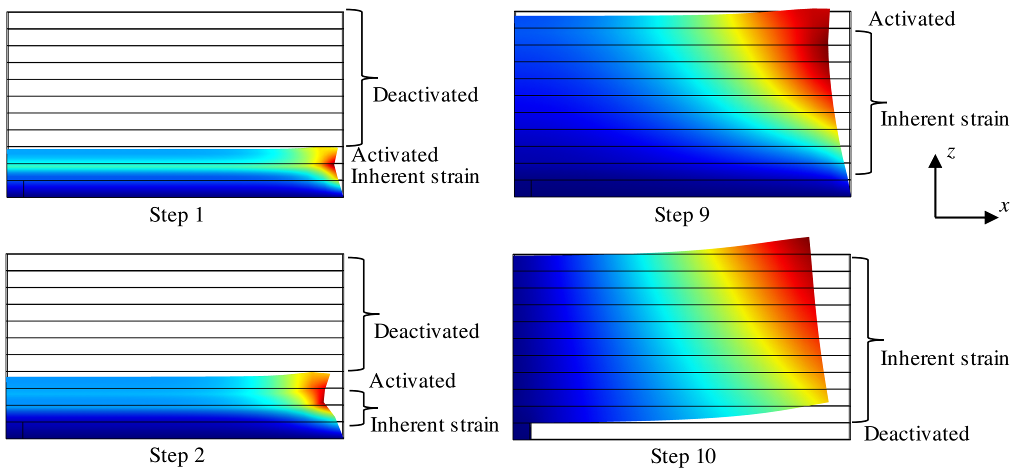

Figure 8: Deformation through inherent strain method including cutting process. The contour represents the magnitude of displacement. The scale factors for deformation diagrams are 50 in steps 1 and 2 and 10 in steps 9 and 10.

4.1.1. Calibration

The concept of an inherent strain is a virtual approximation of the exact welding distortion. Thus, its value must be calibrated based on the exact distortion. In this study, instead of the experiments, the full-scale thermo-mechanical FEM results are obtained using the Simufact Additive (Simufact Engineering Gmbh, Hamburg, Germany). Here, "Full scale" means that the detailed lattice geometry is modeled explicitly in the finite element model without any homogenization method. R1C1 and R3C3: Recently the validity of the full scale thermo-mechanical analysis was confirmed in several works [4, 5, 6, 7, 16]. In this analysis, each lattice is modeled with the exact geometries while is approximated based on the effective values through the inherent strain approach. The geometry is discretized using 1 mm cubic voxel elements. The conditional parameters [4, 6, 16] and temperature-dependent physical properties of the fabrication used in the analysis are summarized in Tables 1, 2, and 3.

Table 1: Process parameters used in the full-scale thermo-mechanical analysis [4, 6, 16].

Parameter name	Value
Laser power [W]	285
Laser absorption efficiency	0.4
Laser scan speed [mm/s]	960
Laser beam diameter [μ m]	100
Layer thickness [μ m]	40
Recoater time [s]	10
Powder and baseplate temperature [°C]	80
Ambient temperature [°C]	25
Surface emissivity	0.3
Natural convection heat transfer coefficient [W/(m^2·°C)]	5

Table 2: Thermal properties of Inconel 718 used in the full-scale thermo-mechanical analysis [4, 6, 16].

Temperature [°C]	Thermal conductivity [W/(m·°C)]	Specific heat [J/kg]	Surface emissivity	Density [kg/m^3]
20	11.4	427	0.3	8146
100	12.5	441	-	-
300	14	481	-	-
500	15.5	521	-	-
700	21.5	601	-	-
1350	31.3	691	-	-

Table 3: Mechanical properties of Inconel 718 used in the detailed thermo-mechanical analysis.

Temperature [°C]	Young's modulus [GPa]	Yield strength [MPa]	Thermal expansion coefficient [$\times 10^{-6}$/°C]
21	208	1172	12.8
93	205	1172	12.8
204	202	-	13.5
316	194	-	13.9
427	186	1089	14.2
538	179	1068	14.4
649	172	1034	15.1
760	162	827	16.1
871	127	286	-
954	17.8	138	16.2

Assuming that the x and y components of the inherent strain, $\varepsilon_x^{\text{ihs}}$ and $\varepsilon_y^{\text{ihs}}$, are identical, the calibration is applied to find the inherent strain values $\varepsilon_x^{\text{ihs}}$ and $\varepsilon_z^{\text{ihs}}$ minimizing the sum of the square error of the z-displacement of the top and bottom planes shown in Fig. 7 between the full-scale thermo-mechanical analysis and the inherent strain method. The inherent strain is updated using the line search method. The design variable is uniformly set to 0.5. R1C1, R2C4, and R3C2: The resulting inherent strains were $\varepsilon_x^{\text{ihs}} = \varepsilon_y^{\text{ihs}} = -6.35 \times 10^{-3}$ and $\varepsilon_z^{\text{ihs}} = -0.85 \times 10^{-3}$ for the Case A lattice and $\varepsilon_x^{\text{ihs}} = \varepsilon_y^{\text{ihs}} = -5.96 \times 10^{-3}$ and $\varepsilon_z^{\text{ihs}} = -0.83 \times 10^{-3}$ for the Case B lattice, respectively. Figure 9 shows the comparison of the deformation diagrams of the detailed analysis and graphs plotting the z-displacement of the top and bottom planes in the Case A lattice. Although the total deformation shapes including the x and y components are different, considering only the

z direction as dominating the warping deformation, an acceptable level of agreement was obtained.

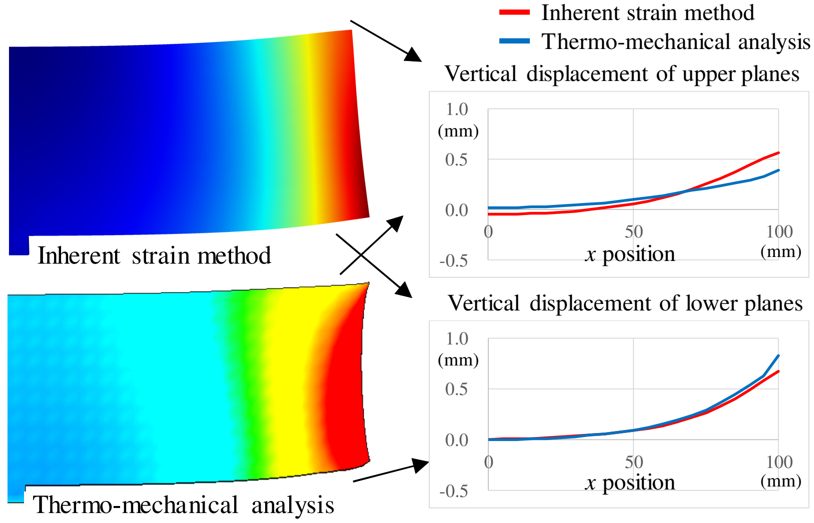

Figure 9: R1C1, R2C4, and R3C2: Comparison of the inherent strain method deformations and the full-scale thermo-mechanical analysis after inherent strain calibration in the Case A lattice. The contour represents the vertical displacement. Scale factors for deformation diagrams are 10.

4.1.2. Validation of sensitivity analysis

R1C1, R2C4, and R3C2: Using the inherent strain of the Case A lattice obtained above, a sensitivity analysis validation is first applied. The analytical sensitivities derived in Eq. (19) are compared with the sensitivities obtained using the finite difference method. The design variable numbering and comparison are shown in Fig. 10. Good agreement was obtained.

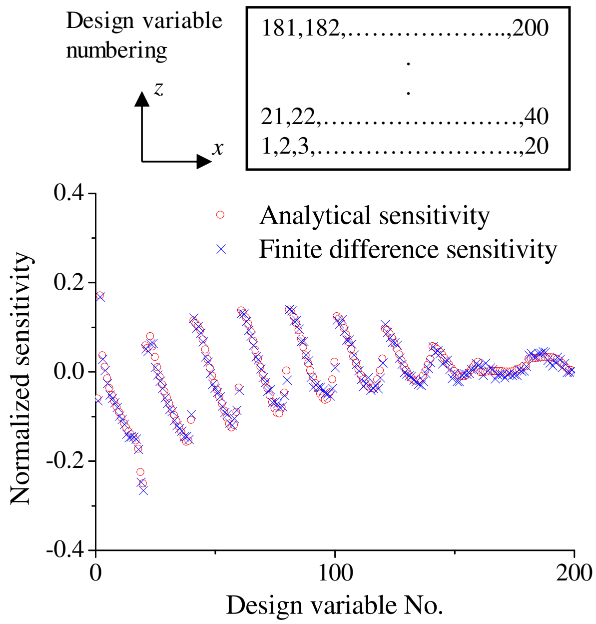

Figure 10: Verification of the analytical sensitivity through a comparison with the finite difference sensitivity.

4.1.3. Optimization

A lattice density optimization is then conducted. R1C1, R2C4, and R3C2: The initial design variable is uniformly set to 0.5, corresponding to a volume fraction of approximately 83% and 87% in the Cases A and B lattices respectively. Figure 11 shows the iteration histories of the objective function and the average lattice volume fraction in the Case A lattice. A smooth and sufficient convergence is obtained until 30 iterations. The total volume of the optimal result becomes smaller than the initial value. Figure 12 shows a 2D optimal distribution of the design variables and a 3D view of the corresponding geometry. Denser lattices are laid out on the lower layer in both lattice cases. As shown in Fig. 2, high strains are given for the layer near the top owing to the effect of the activation. Because of the internal stress, which causes a bending deformation, is given by multiplying the stiffness and strain, by weakening the upper layer stiffness, the internal upper layer stress is also reduced. As a result, an arch-like distribution is formed. The converged objective function values of the Cases A and B lattices were 5.18×10^{-12} and 8.68×10^{-12}, respectively. This indicates the larger gap between the minimum and maximum stiffness of the lattice works better. R2C5: The isolated dense lattices were observed on the right top side in both lattice cases. The re-analysis results after making their design variables zero show just 0.06% and -0.01% objective function changes in the Cases A and B lattices, respectively. According to the history of the lattice density shown in Fig. 11, the right upper side lattices were important only in the early stages of optimization and the surrounding lattices were vanished through the optimization. Due to the lack of volume constraint, such unnecessary lattices can remain in this optimization. Practically, these lattices can be ignored.

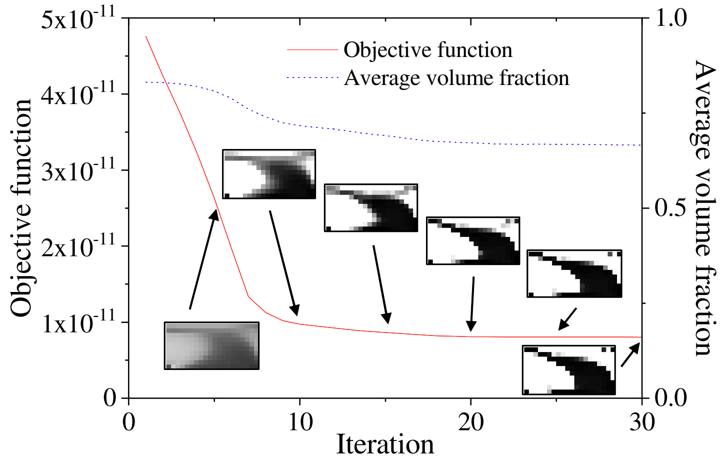

Figure 11: R2C5: Convergence history of the objective function and average volume fraction of the lattices in Case A lattice optimization. Intermediate optimal lattice density distributions are also shown after each five iterations.

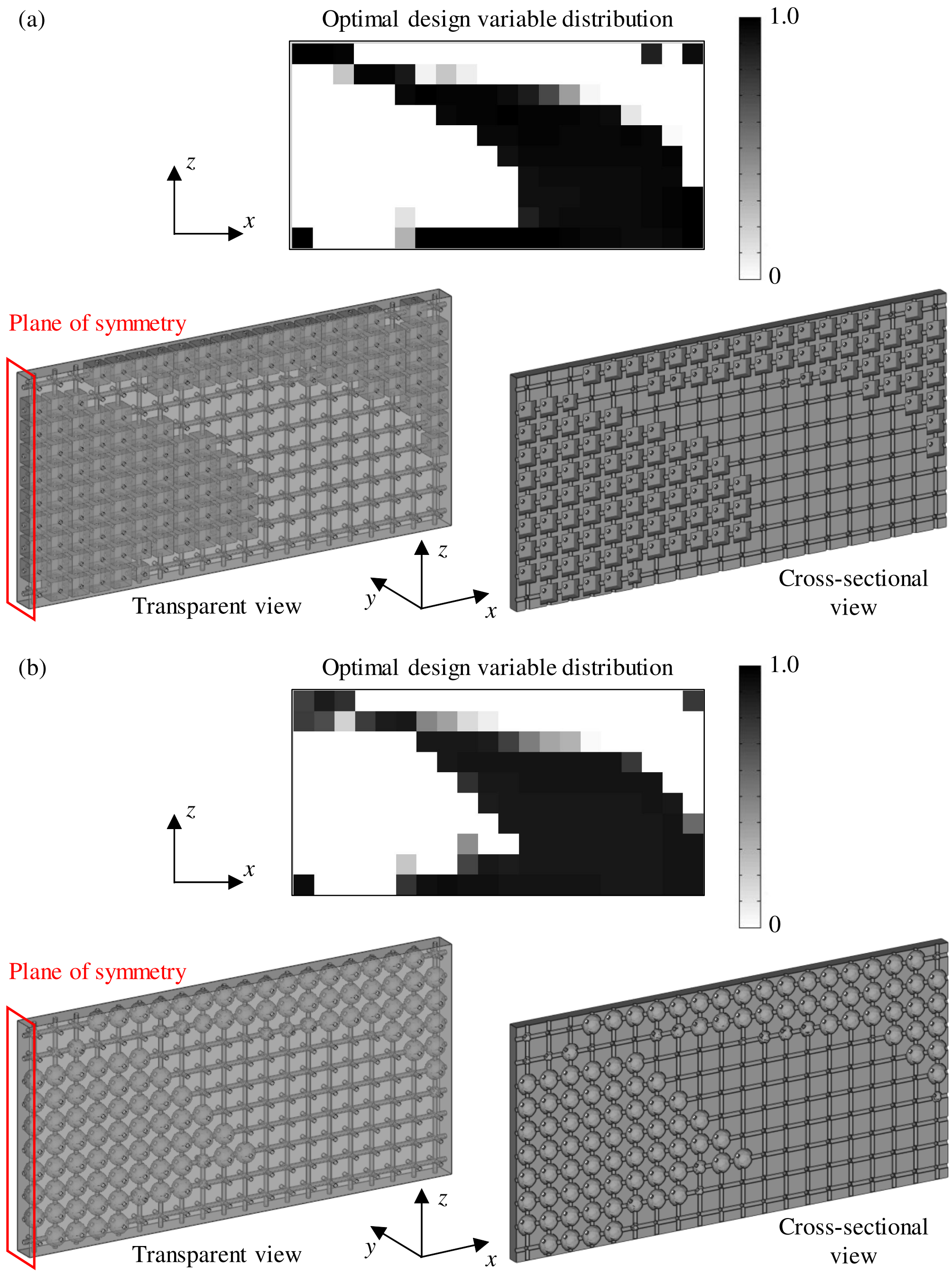

Figure 12: R1C1, R2C4, and R3C2: Optimal distribution of the design variable and corresponding detailed geometry of (a) Case A and (b) Case B.

Figure 13 shows a comparison of the vertical deformation between the optimal and uniform lattice structure having the same volume fraction using the inherent strain method and the full-scale thermo-mechanical analysis. A smaller vertical deformation is clearly obtained on both the top and bottom planes through the inherent strain method. A full-scale thermo-mechanical analysis is conducted using the Simufact Additive software, same with the calibration. Although the deformation of the optimal lattice structure is sharper than the inherent strain analysis on the bottom plane, a smaller displacements were clearly obtained in both cases. The optimal results obtained by the inherent strain method can also be applied in the full-scale thermo-mechanical analysis. R3C1: The computational time of the inherent strain method and the full-scale analysis are 83.6 s and 9,225.5 s, respectively, using an Intel Core i7-8750H processor (six cores) and 32 GB memory. The full-scale analysis computational time is certainly not acceptable for structural optimization as reported in [14] and [16].

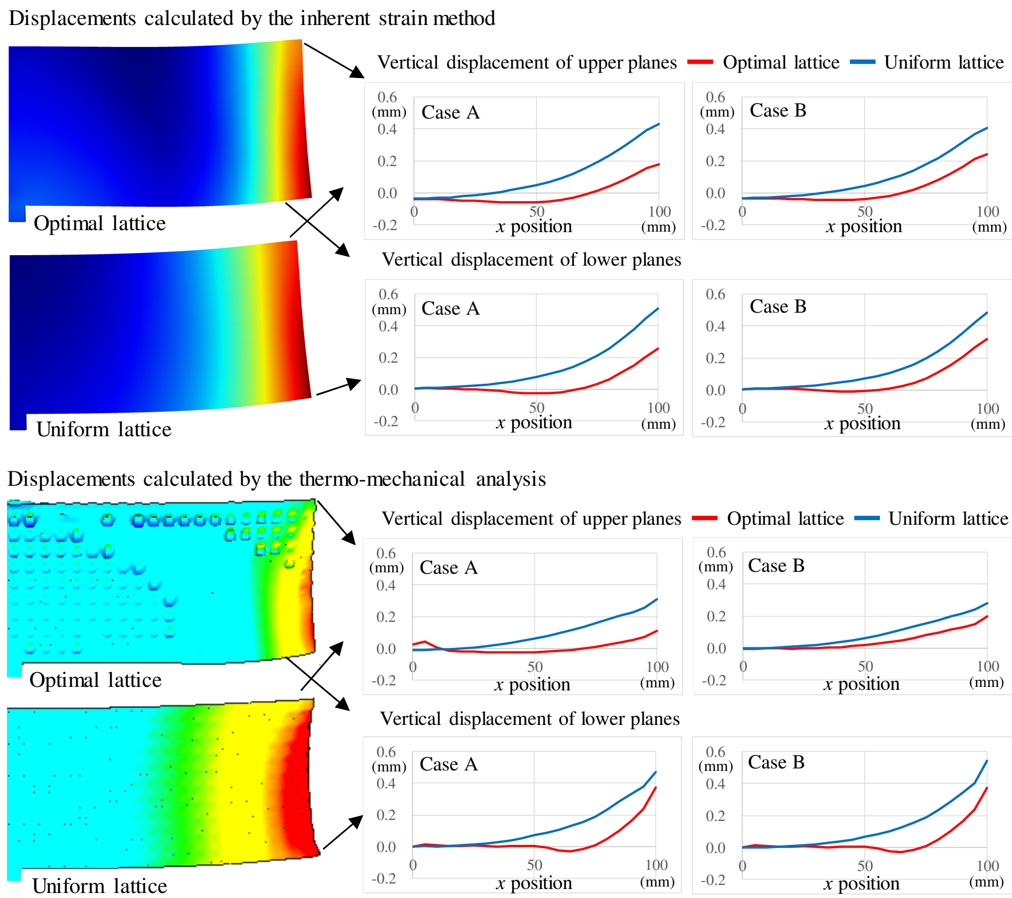

Figure 13: R1C1, R2C4, and R3C2: Comparison of the vertical displacement between the optimal lattice structure and the uniform lattice structure using the inherent strain method and the full-scale thermo-mechanical analysis. The contour represents the vertical displacement. The deformation diagrams are the results of the Case A lattice with a scale factor of 10.

4.2. 3D example

Figure 14 shows the design target of the structure of a 3D example. Considering the fabrication of a 200 mm $\times$ 200 mm $\times$ 50 mm rectangular shape composed of ten inherent strain layers, the vertical displacements of its upper and lower layers are minimized. Similar to the 2D example, the bottom 5 mm layer assumes a base plate with a fully dense material. Considering the post-processing cutting of the bottom of the part after fabrication, excluding the left bottom corner lattice, as shown in Fig. 14, we evaluate the sum of the square of the vertical displacements of the top and bottom part planes as the objective function. The analysis domain is one-quarter of the entire structure when considering the symmetry. The domain is discretized using a 5 mm voxel element, which corresponds to one 5 mm lattice. Thus, the part domain is composed of 20 × 20 × 10 lattices. R1C1, R2C4, and R3C2: The lattices are assumed to be Case A whose initial design variables are uniformly set to 0.5.

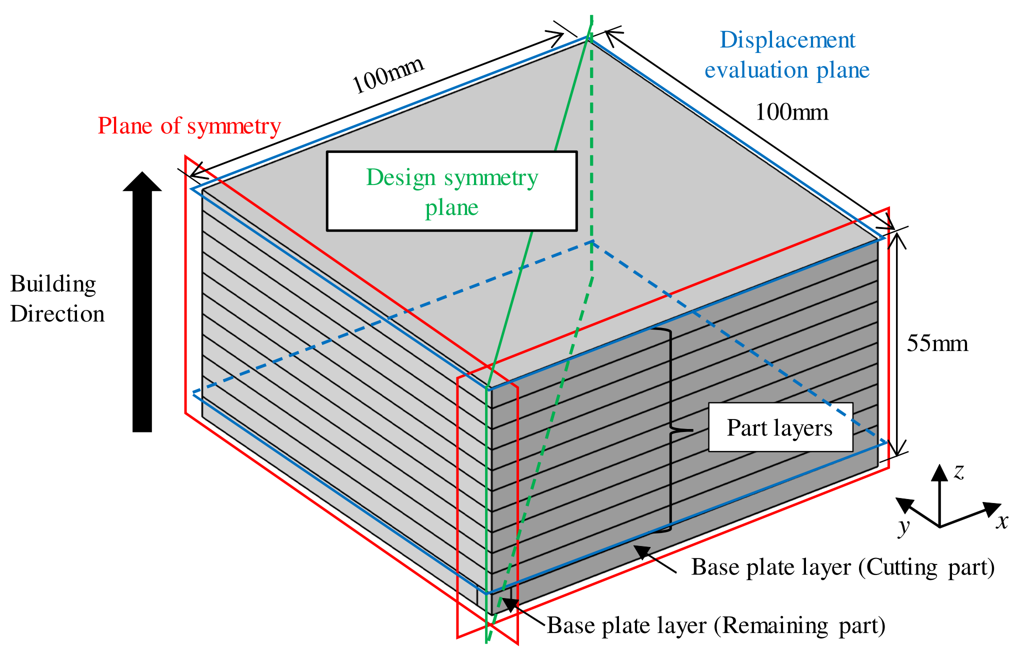

Figure 14: Outline of design target of the quasi 3D example.

Figure 15 shows the optimal distribution of the design variable and a 3D view of the corresponding geometry obtained after 50 iterations. The design variables and detailed shapes of the cross-sections are also shown. Similar with the 2D model, an arch-like distribution of dense lattices is formed over the domain. Figure 16 shows a comparison of the vertical deformation between the optimal and uniform lattice structures having same volume fraction when using the inherent strain method and the full-scale thermo-mechanical analysis. In the full-scale thermo-mechanical analysis, the domain is discretized using a 2.5 mm voxel mesh, which is coarser than in the 2D example. In both results, optimal results are clearly achieved at a lower displacement than with a uniform lattice structure. The proposed method was valid, even in the 3D study. R3C1: The computational time of the inherent strain method and the full-scale analysis are 83.6 s and 14,614.9 s, respectively, under the same computational environment with the 2D example.

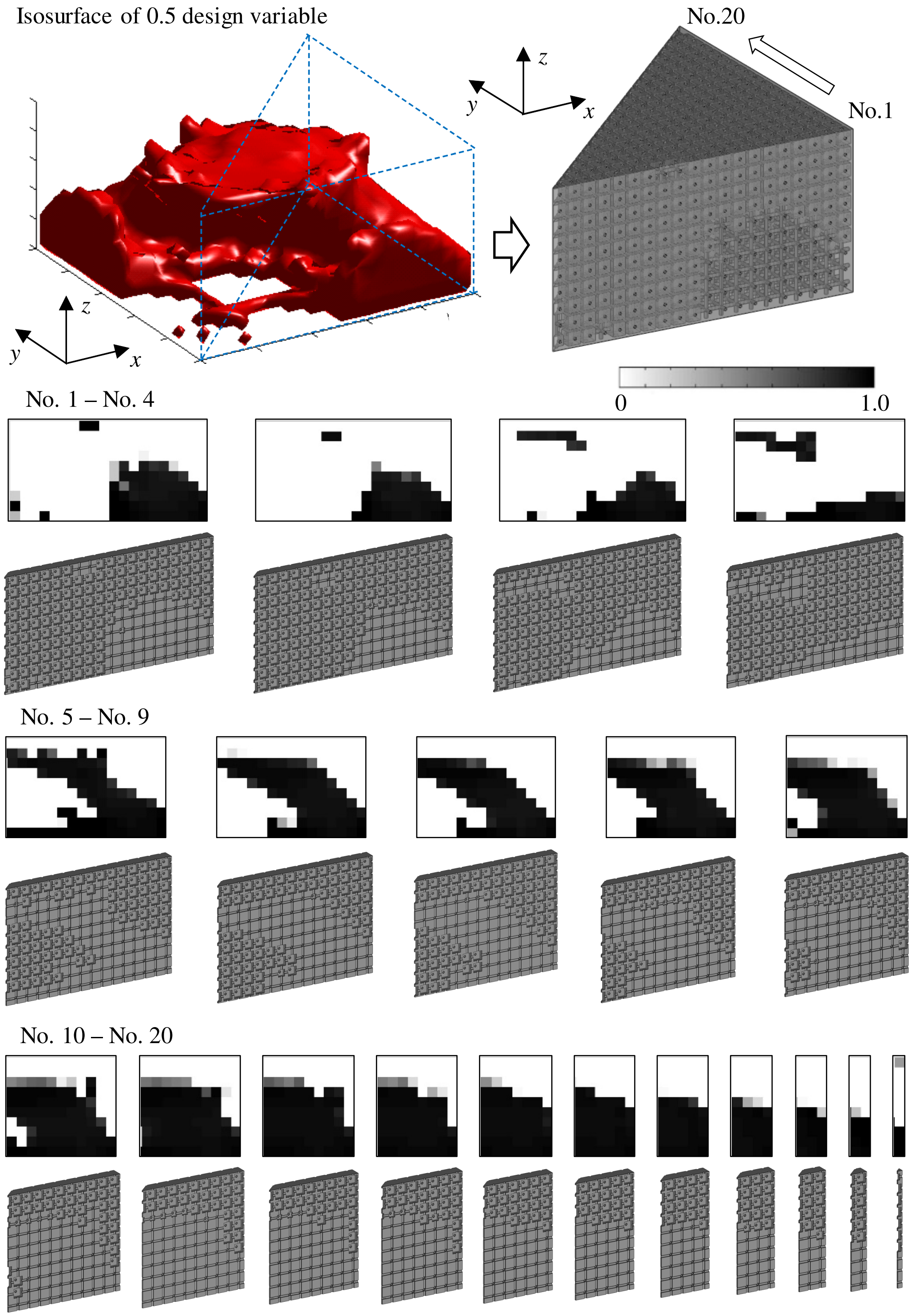

Figure 15: Optimal distribution of design variables and corresponding detailed geometry.

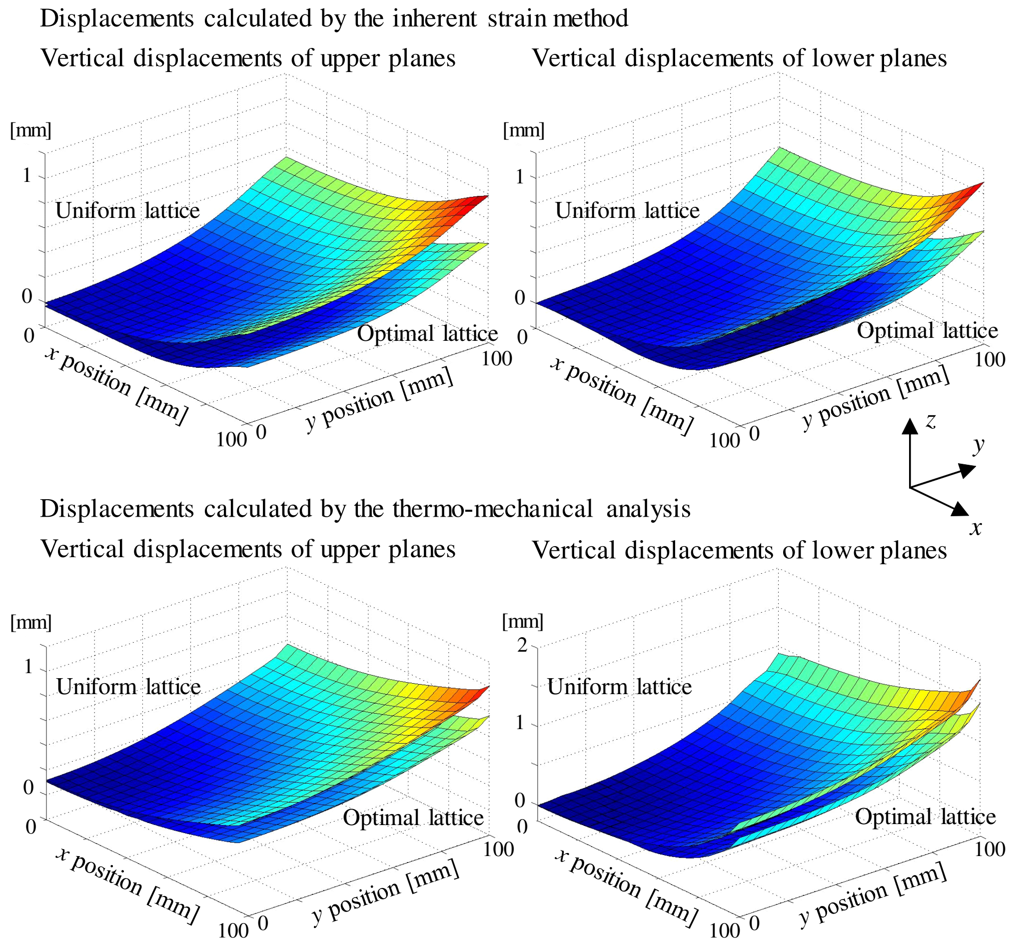

Figure 16: Comparison of the vertical displacement between the optimal lattice structure and the uniform lattice structure using the inherent strain method and the full-scale thermo-mechanical analysis.

5. Conclusion

We studied the optimization of the lattice structure distribution for a minimization of the thermal distortion based on the layer-by-layer inherent strain method. The inherent strain process representing the stack of the strain from the layer-by-layer process was formulated through the activation of elements in the recurrent formula. A sensitivity analysis was conducted for this recurrent formula. A cubic lattice with a cubic void was assumed as the base shape of the lattice, and its effective elastic tensor was derived using a numerical homogenization method. The design variables were related with the size and volume fractions of the lattice and updated using the MMA. The proposed method was examined by solving quasi 2D and 3D numerical examples.

The calibration and verification of the proposed method were conducted using a full-scale thermo-mechanical analysis. R1C1 and R3C3: Although the validity of the full scale thermo-mechanical analysis was confirmed in several works [4, 5, 6, 7, 16], for a more strict and practical verification, experimental studies are being planned for the proposed method. R2C2: Moreover, the assumption that the inherent strain is uniform in every layer is insufficient for an approximation of the lattice structure deformation because the laser path and the resulting thermal distortion can vary according to the geometry change of the lattice. This was found in the gap in the displacements between the inherent strain method and full-scale thermo-mechanical analysis. The development of more accurate inherent strain methods whose inherent strain values are depending on the lattice density is an important issue for improvement of the proposed method. If a more accurate displacement prediction can be achieved for a complicated distribution of the lattice, the design of the arbitrary thermal distortion can be achieved along with its minimization.

Acknowledgments

This work was partially supported by the JSPS KAKENHI (18H01351, 18KK0412 and 19H05625) and the JST, A-Step, Seeds development type (JPMJTR192A). Partial financial support from the U.S. National Science Foundation (CMMI-1634261) is also gratefully acknowledged.

Appendix A. Study on imperfect sensitivity analysis when considering only the final state.

To confirm the necessity of considering the entire layer-by-layer process of the inherent strain method in its sensitivity analysis, an optimization through an imperfect sensitivity is described in this appendix. Here, using the equilibrium equation of the final state $\mathbf{Ku} = \mathbf{f}$ after cutting, the sensitivity of an orbital objective function $g(\mathbf{u})$ is derived as $\dfrac{dg}{dx} = \dfrac{\partial g}{\partial x} + \boldsymbol{\lambda}^T \dfrac{\partial \mathbf{K}}{\partial x}\mathbf{u}$, where $\dfrac{\partial g}{\partial \mathbf{u}} + \boldsymbol{\lambda}^T \mathbf{K} = \mathbf{0}$. The dependency of the design variable on the force is ignored because it cannot be explicitly derived through this approach.

R1C1, R2C4, and R3C2: Figure A.17 shows the optimal distribution of the quasi 2D problem shown in Fig. 7 obtained using the above sensitivity, the Case A lattice, and the same settings described in Section 4.1.3. The resulting objective function value is 260.2% higher than the optimal result with a perfect sensitivity analysis. Figure A.18 shows the verification of this result through the full-scale thermo-mechanical analysis. These results indicate that considering only the final state is insufficient for minimizing the distortion if it is not dominated by the final state.

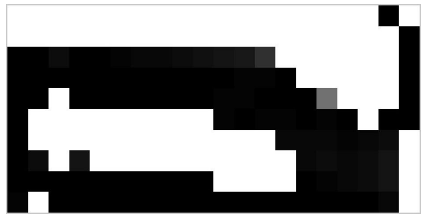

Figure A.17: Optimal distribution of design variables obtained from an imperfect sensitivity.

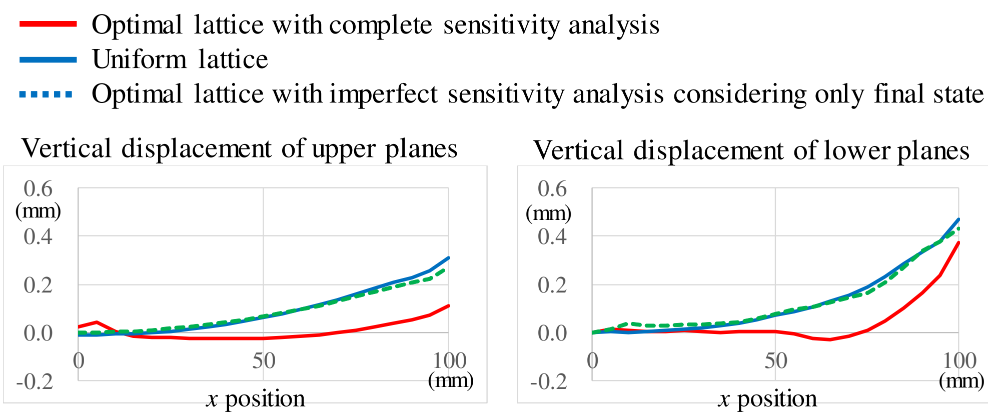

Figure A.18: Verification of the optimal lattices obtained from an imperfect sensitivity using the full-scale thermo-mechanical analysis.

References

[1] I. Gibson, D. Rosen, B. Stucker, Additive manufacturing technologies, Springer, 2010.

[2] P. Mercelis, J. P. Kruth, Residual stresses in selective laser sintering and selective laser melting, Rapid Prototyp. J. 12 (5) (2006) 254–265.

[3] A. S. Wu, D. W. Brown, M. Kumar, G. F. Gallegos, W. E. King, An experimental investigation into additive manufacturing-induced residual

stresses in 316l stainless steel, Metall. Mater. Trans. 45 (13) (2014) 6260–6270.

[4] A. J. Dunbar, E. R. Denlinger, M. F. Gouge, P. Michaleris, Experimental validation of finite element modeling for laser powder bed fusion deformation, Addit. Manufact. 12 (2016) 108–120.

[5] S. Afazov, W. A. D. Denmark, B. L. Toralles, A. Holloway, A. Yaghi, Distortion prediction and compensation in selective laser melting, Addit. Manufact. 17 (2017) 15–22.

[6] E. R. Denlinger, M. Gouge, J. Irwin, P. Michaleris, Thermomechanical model development and in situ experimental validation of the laser powder-bed fusion process, Addit. Manufact. 16 (2017) 73–80.

[7] M. Schänzel, D. Shakirov, A. Ilin, V. Ploshikhin, Coupled thermo-mechanical process simulation method for selective laser melting considering phase transformation steels, Comput. Math. Appl. 78 (7) (2019) 2230–2246.

[8] E. F. Rybicki, D. W. Schmueser, R. W. Stonesifer, J. J. Groom, H. W. Mishler, A finite-element model for residual stresses and deflections in girth-butt welded pipes, J. Pressure Vessel Technol 100 (3) (1978) 256–262.

[9] L.-E. Lindgren, H. Runnemalm, M. O. Näsström, Simulation of multipass welding of a thick plate, Int. J. Numer. Meth. Eng. 44 (9) (1999) 1301–1316.

[10] L. E. Lindgren, Computational welding mechanics, Elsevier, 2007.

[11] N. Keller, V. Ploshikhin, New method for fast predictions of residual stress and distortion of am parts, in: Proceedings of the 25th Annual International Solid Freeform Fabrication Symposium, 2014, pp. 1229–1237.

[12] N. Keller, Verzugsminimierung bei selektiven laserschmelz-verfahren durch multi-skalen-simulation, Ph.D. thesis, Universität Bremen (2016).

[13] M. Bugatti, Q. Semeraro, Limitations of the inherent strain method in simulating powder bed fusion processes, Addit. Manufact. 23 (2018) 329–346.

[14] X. Liang, L. Cheng, Q. Chen, Q. Yang, A. C. To, A modified method for estimating inherent strains from detailed process simulation for fast residual distortion prediction of single-walled structures fabricated by directed energy deposition, Addit. Manufact. 23 (2018) 471–486.

[15] I. Setien, M. Chiumenti, S. van der Veen, M. San Sebastian, F. Garciandía, A. Echeverría, Empirical methodology to determine inherent strains in additive manufacturing, Comput. Math. Appl. 78 (7) (2019) 2282–2295.

[16] Q. Chen, X. Liang, D. Hayduke, J. Liu, L. Cheng, J. Oskin, R. Whitmore, A. C. To, An inherent strain based multiscale modeling framework for simulating part-scale residual deformation for direct metal laser sintering, Addit. Manufact. 28 (2019) 406–418.

[17] A. M. Mirzendehdel, B. Rankouhi, K. Suresh, Strength-based topology optimization for anisotropic parts, Addit. Manufact. 19 (2018) 104–113.

[18] Y. Liu, Z. Li, P. Wei, S. Chen, Generating support structures for additive manufacturing with continuum topology optimization methods, Rapid Prototyp. J. 25 (2) (2019) 232–246.

[19] L. Cheng, X. Liang, J. Bai, Q. Chen, J. Lemon, A. To, On utilizing topology optimization to design support structure to prevent residual stress induced build failure in laser powder bed metal additive manufacturing, Addit. Manufact. 27 (2019) 290–304.

[20] L. Ryan, I. Y. Kim, A multiobjective topology optimization approach for cost and time minimization in additive manufacturing, Int. J. Numer. Meth. Eng. 118 (7) (2019) 371–394.

[21] M. Seabra, J. Azevedo, A. Araújo, L. Reis, E. Pinto, N. Alves, R. Santos, J. P. Mortágua, Selective laser melting (slm) and topology optimization for lighter aerospace componentes, Procedia Structural Integrity 1 (2016) 289–296.

[22] C. H. Chuang, S. Chen, R. J. Yang, P. Vogiatzis, Topology optimization with additive manufacturing consideration for vehicle load path development, Int. J. Numer. Meth. Eng. 113 (8) (2018) 1434–1445.

[23] S. J. Hollister, Porous scaffold design for tissue engineering, Nat. Mater. 4 (7) (2005) 518–524.

[24] C. Y. Lin, T. Wirtz, F. LaMarca, S. J. Hollister, Structural and mechanical evaluations of a topology optimized titanium interbody fusion

cage fabricated by selective laser melting process, J. Biomed. Mater. Res. 83 (2) (2007) 272–279.

[25] D. Xiao, Y. Yang, X. Su, D. Wang, J. Sun, An integrated approach of topology optimized design and selective laser melting process for titanium implants materials, Bio-Med. Mater. Eng. 23 (5) (2013) 433–445.

[26] Y. Koizumi, A. Okazaki, A. Chiba, T. Kato, A. Takezawa, Cellular lattices of biomedical co-cr-mo-alloy fabricated by electron beam melting with the aid of shape optimization, Addit. Manufact. 12B (2016) 305–313.

[27] A. Takezawa, Y. Koizumi, M. Kobashi, High-stiffness and strength porous maraging steel via topology optimization and selective laser melting, Addit. Manufact. 18 (2017) 194–202.

[28] A. Takezawa, M. Kobashi, Y. Koizumi, M. Kitamura, Porous metal produced by selective laser melting with effective isotropic thermal conductivity close to the hashin–shtrikman bound, Int. J. Heat. Mass. Tran. 105 (2017) 564–572.

[29] J. Schwerdtfeger, F. Wein, G. Leugering, R. F. Singer, C. Körner, M. Stingl, F. Schury, Design of auxetic structures via mathematical optimization, Adv. Mater. 23 (22-23) (2011) 2650–2654.

[30] E. Andreassen, B. S. Lazarov, O. Sigmund, Design of manufacturable 3d extremal elastic microstructure, Mech. Mater. 69 (1) (2014) 1–10.

[31] A. Clausen, F. Wang, J. S. Jensen, O. Sigmund, J. A. Lewis, Topology

optimized architectures with programmable poisson's ratio over large deformations, Adv. Mater. 27 (37) (2015) 5523–5527.

[32] A. Takezawa, M. Kobashi, M. Kitamura, Porous composite with negative thermal expansion obtained by photopolymer additive manufacturing, APL Mater. 3 (7) (2015) 076103.

[33] A. Takezawa, M. Kobashi, Design methodology for porous composites with tunable thermal expansion produced by multi-material topology optimization and additive manufacturing, Compos. B Eng. 131 (2017) 21–29.

[34] Y. Miyamoto, W. A. Kaysser, B. H. Rabin, A. Kawasaki, R. Ford, Functionally graded materials: design, processing and applications, Springer Science & Business Media, 2013.

[35] S. A. Khanoki, D. Pasini, Multiscale design and multiobjective optimization of orthopedic hip implants with functionally graded cellular material, J. Biomech. Eng. 134 (3) (2012) 031004.

[36] P. Zhang, J. Toman, Y. Yu, E. Biyikli, M. Kirca, M. Chmielus, A. C. To, Efficient design-optimization of variable-density hexagonal cellular structure by additive manufacturing: Theory and validation, ASME J. Manuf. Sci. Eng. 137 (2) (2015) 021004.

[37] L. Cheng, P. Zhang, E. Biyikli, J. Bai, J. Robbins, A. To, Efficient design optimization of variable-density cellular structures for additive manufacturing: theory and experimental validation, Rapid Prototyp. J. 23 (4) (2017) 660–677.

[38] L. Cheng, J. Bai, A. C. To, Functionally graded lattice structure topology optimization for the design of additive manufactured components with stress constraints, Comput. Meth. Appl. Mech. Eng. 344 (2019) 334–359.

[39] C. L. Lynch M. E., Mordasky M., T. A., Design, testing, and mechanical behavior of additively manufactured casing with optimized lattice structure, Addit. Manufact. 22 (2018) 462–471.

[40] A. Clausen, N. Aage, O. Sigmund, Exploiting additive manufacturing infill in topology optimization for improved buckling load, Engineering 2 (2) (2016) 250–257.

[41] X. Wang, P. Zhang, S. Ludwick, E. Belski, A. C. To, Natural frequency optimization of 3d printed variable-density honeycomb structure via a homogenization-based approach, Addit. Manufact. 20 (2018) 189–198.

[42] L. Cheng, X. Liang, E. Belski, X. Wang, J. M. Sietins, S. Ludwick, A. To, Natural frequency optimization of variable-density additive manufactured lattice structure: Theory and experimental validation, J. Manuf. Sci. Eng. 140 (10) (2018) 105002.

[43] L. Cheng, J. Liu, X. Liang, A. C. To, Coupling lattice structure topology optimization with design-dependent feature evolution for additive manufactured heat conduction design, Comput. Meth. in Appl. Mech. and Eng. 332 (2018) 408–439.

[44] L. Cheng, J. Liu, A. C. To, Concurrent lattice infill with feature evo-

lution optimization for additive manufactured heat conduction design, Struct. Multidisc. Optim. (2018) 1–25.

[45] A. Takezawa, X. Zhang, M. Kato, M. Kitamura, Method to optimize an additively-manufactured functionally-graded lattice structure for effective liquid cooling, Addit. Manufact. 28 (2019) 285–298.

[46] A. Takezawa, X. Zhang, M. Kitamura, Optimization of an additively manufactured functionally graded lattice structure with liquid cooling considering structural performances, Int. J. Heat Mass Trans. 143 (2019) 118564.

[47] P. G. Coelho, P. R. Fernandes, J. M. Guedes, H. C. Rodrigues, A hierarchical model for concurrent material and topology optimisation of three-dimensional structures, Struct. Multidisc. Optim. 35 (2) (2008) 107–115.

[48] L. Liu, J. Yan, G. Cheng, Optimum structure with homogeneous optimum truss-like material, Comput. Struct. 86 (13-14) (2008) 1417–1425.

[49] E. J. Haug, K. K. Choi, V. Komkov, Design Sensitivity Analysis of Structural Systems, Academic Press, Orlando, 1986.

[50] J. M. Guedes, N. Kikuchi, Preprocessing and postprocessing for materials based on the homogenization method with adaptive finite element methods, Comput. Meth. Appl. Mech. Eng. 83 (2) (1990) 143–198.

[51] E. Andreassen, C. S. Andreasen, How to determine composite material properties using numerical homogenization, Comput. Mater. Sci. 83 (2014) 488–495.

[52] K. Svanberg, The method of moving asymptotes- a new method for structural optimization, Int. J. Numer. Meth. Eng. 24 (2) (1987) 359–373.

[53] Y. Ueda, M. G. Yuan, Prediction of residual stresses in butt welded plates using inherent strains, J. Eng. Mater. Tech. 115 (4) (1993) 417–423.

[54] W. Liang, D. Deng, S. Sone, H. Murakawa, Prediction of welding distortion by elastic finite element analysis using inherent deformation estimated through inverse analysis, Weld. World 49 (11-12) (2005) 30–39.

[55] D. Deng, H. Murakawa, W. Liang, Numerical simulation of welding distortion in large structures, Comput. Meth. Appl. Mech. Eng. 196 (45-48) (2007) 4613–4627.

[56] H. Murakawa, D. Deng, N. Ma, J. Wang, Applications of inherent strain and interface element to simulation of welding deformation in thin plate structures, Comput. Mater. Sci. 51 (1) (2011) 43–52.

[57] M. P. Bendsøe, N. Kikuchi, Generating optimal topologies in structural design using a homogenization method, Comput. Meth. Appl. Mech. Eng. 71 (2) (1988) 197–224.

[58] M. P. Bendsøe, O. Sigmund, Topology Optimization: Theory, Methods, and Applications, Springer-Verlag, Berlin, 2003.

Declarationof interests

☒ The authors declare that they have no known competing financial interests or personal relationships that could have appeared to influence the work reported in this paper.

☐The authors declare the following financial interests/personal relationships which may be considered as potential competing interests: